Supporting Information

Site-resolved measurement of microsecond to millisecond conformational-exchange processes in proteins by solid-state NMR spectroscopy

Martin Tollinger, Astrid C. Sivertsen, Beat H. Meier, Matthias Ernst and Paul Schanda

Table of Contents

NUMERICAL SIMULATIONS OF THE DIFFERENTIAL MQC DECAY IN A ROTATING SOLID SAMPLE

Here we investigate the properties of the differential ZQ/DQ line broadening under a number of exchange scenarios.

We first show that both the isotropic (CSM/CSM) and the anisotropic component (CSA/CSA) of the chemical-shift tensor lead to differential line broadening, and that their effect is additive (Figure S1, and Figure 1 of main paper). The time scales at which the differential broadening effects are maximum are different for the two mechanisms. In the case of the CSM/CSM mechanism, sizeable differential broadening is observed when the exchange rate of the process is in the range of 10^3 to 10^6 s^{-1}. These values depend on the exact chemical-shift differences. This effect has been discussed elsewhere for the case of solution-state NMR,[1] and our simulations of the CSM/CSM mechanism in the solid state under MAS lead to the same results as their analytical expressions, which were used to calculate the data in the insert in Figure S1.

The CSA/CSA mechanism is most active at a faster time scale, as shown in Figure S1. The exact rate dependence of this mechanism varies with the nature of the dynamic process (jump model, angles, CSA parameters). Via the CSA/CSA mechanism, differential line broadening is not only induced for the case of jumps between distinct conformations, but also for (restricted) rotational diffusion, which influences the CSA tensor orientations. In addition, this mechanism is sensitive to a change in the anisotropy or asymmetry parameter of the CSA tensor. It is an interference effect between the periodic modulation of the CSA tensor by MAS and the stochastic modulation of the CSA tensor by the dynamic process. We show this with two different models in Figure S2. First, we simulate a two-site exchange process between equally populated states differing only in the orientations of the CSA tensors. As expected, this leads to differential MQC decay in a similar manner as in the 9:1 exchange scenario of Figure S1. In addition, we calculated the differential relaxation-rate constant within the framework of Redfield theory (Figure S3). Although the validity of the Redfield theory breaks down for slow motions (slower than about 10^6 s^{-1}) our calculations show that the fast branch of the ΔR_{MQ} curves can be understood as a Redfield relaxation process.

Further simulations show the possible origins of negative values of ΔR_{MQ}. Negative values can arise either if the product of the two *isotropic* chemical shift changes is negative (Figure S3), or if the sign of the *anisotropy* of one of the CSAs changes upon the exchange process (not shown), or if the angular fluctuations of the two CSAs are anti-correlated (Figure S4).

Finally, we show that the CSA/CSA-induced differential line broadening is MAS dependent, but not the broadening induced by the CSM/CSM mechanism (Figure S5).

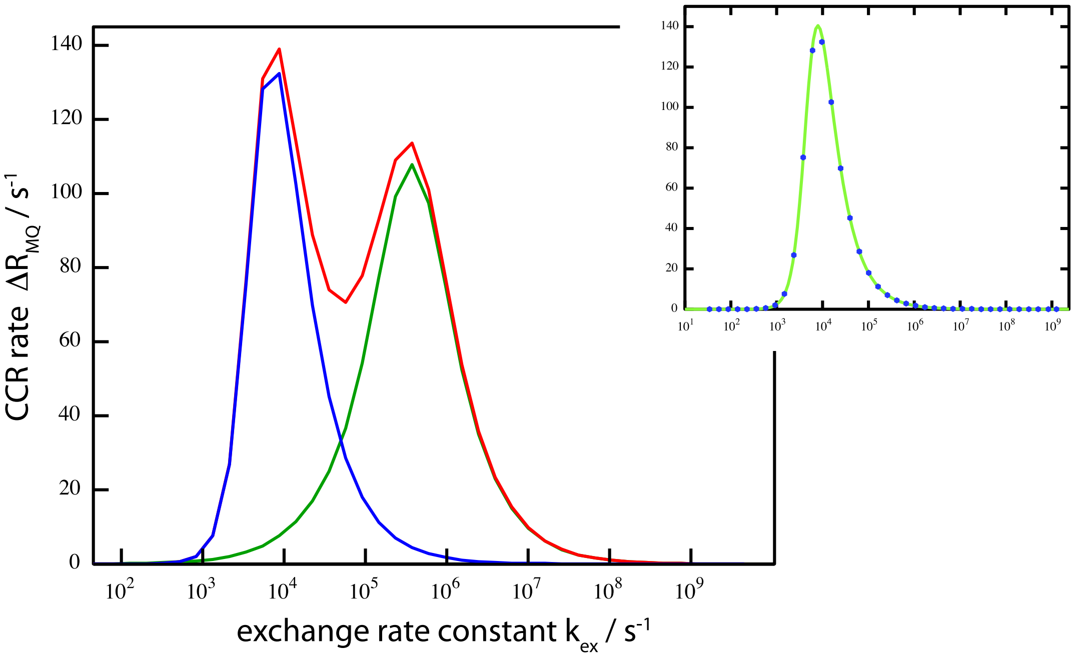

Figure S1. Differential zero- and double quantum line broadening $\Delta R_{MQ}=R_{DQ}-R_{ZQ}$ of ^{1}H-^{15}N arising from either correlated *isotropic* chemical-shift modulation (blue), correlated *anisotropic* chemical-shift modulation (green) or both (red).

In all simulations, a two-spin system (N-H) was assumed, with a dipolar coupling of 22.5kHz (1.02Å bond length). The CSA of ^{15}N was assumed as axially symmetric (i.e. asymmetry $\eta=\sigma_{yy}-\sigma_{xx})/\sigma_{zz}=0$), with its principal axis aligned along the N-H bond (angle β=0). The tensor asymmetry was set to σ_{zz}=113ppm (Δσ=170ppm), at a B_0 field corresponding to 800MHz ^{1}H Larmor frequency. The ^{1}H CSA was assumed as asymmetric (η=0.9) with σ_{zz}=6ppm. In the major conformation the angle of the ^{1}H CSA tensor was β=10° relative to the N-H bond, which was assumed to coincide with the angle β of the ^{15}N CSA tensor. These tensor parameters are in the typical range found in proteins.[1-3] The MAS frequency was set to 50kHz in all simulations in this figure as well as in Figures S3-S5. (The MAS dependency is shown in Figure S5.)

This systems was undergoing exchange between a major (p_a=90%) and a minor (p_b=10%) conformation, with forward and backward rates of k_{ab} and $k_{ba}=p_a/p_b *k_{ab}$, and the following properties that alter between the two conformations.

In the first scenario (blue), the bond angle and the CSA tensors were fixed, and equal in both conformations, and only a difference in isotropic chemical shift was assumed ($\Delta\nu_N$=160Hz, $\Delta\nu_H$=800Hz, i.e. 2ppm and 1ppm, respectively on a 18.8T magnet).

In a second scenario (green), the isotropic chemical shift difference between major and minor state was zero for ^{1}H and ^{15}N, and only the angle of the CSA tensors and dipolar coupling changed upon the exchange process by an angle of 30°, i.e. β (^{1}H CSA)=40°, β (^{15}N CSA)=30°, β (^{1}H-^{15}N dipolar tensor)=30°. (Note that the variation of the angle of the dipolar coupling does not influence the outcome, and identical results are obtained even if the coupling is eliminated.)

In a third scenario (red), both the isotropic and anisotropic chemical shift were modulated upon exchange.

The insert on the top right shows the agreement of the numerical simulation, taking only into account the isotropic chemical shift differences (cf. blue curve in main panel), with the analytical equation for the differential line broadening, as reported previously.[1,4] As shown by this agreement, the CSM/CSM mechanism can be fully understood by previously developed theory.[1,5,6]

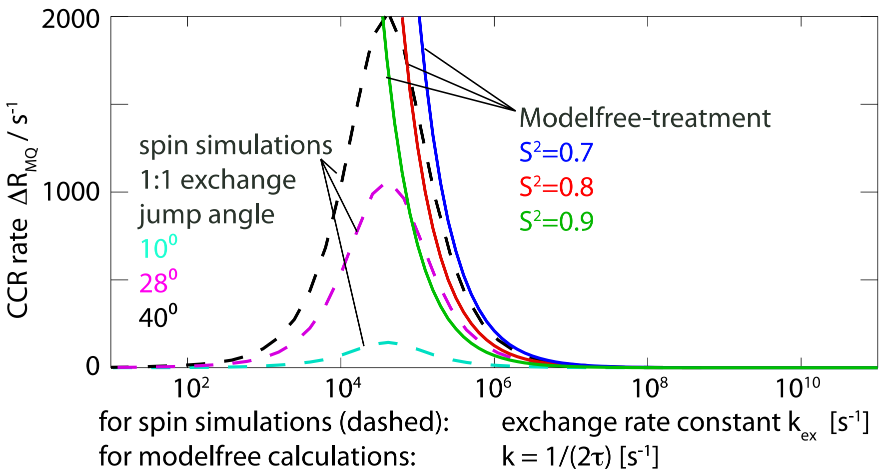

Figure S2. Redfield treatment of the differential ZQ/DQ decay.
Cross-correlated relaxation rates of differential zero- and double-quantum relaxation were calculated according to Redfield theory. The expression for the differential relaxation rate, ΔR_{MQ} is:[7]

$$\Delta R_{MQ} = R_{DQ} - R_{ZQ} = \frac{\delta^2}{32}\left(12J(\omega_H+\omega_N) - 2J(\omega_H-\omega_N)\right) + 2(\omega_N\Delta\sigma_N)(\omega_H\Delta\sigma_H)J(0)$$

where the dipolar coupling is $\delta_D = \frac{-2\mu_0}{4\pi}\frac{\gamma_H\gamma_N\hbar}{r_{NH}^3}$, ω_N and ω_H are the Larmor frequencies of ^{15}N and ^1H, and $\Delta\sigma$ is the difference of the parallel and perpendicular components of the CSA tensors, which are assumed to be axially symmetric. The spectral density functions, J, were calculated using the Modelfree approach,[8] but neglecting overall tumbling: $J(\omega) = 2/5\cdot(1-S^2)\cdot\tau/(1+\tau^2\omega^2)$. Internal motion with an order parameter of S^2=0.7 to 0.9 (as indicated) was considered. For illustration, we compare these calculations with numerical spin simulations with stochastic jumps between two equally populated conformations. It must be noted that the Modelfree treatment is not strictly valid for a rotating sample.[9-11] Furthermore, as also shown by the discrepancy between the Redfield treatment and the numerical simulations, the validity of the Redfield treatment is not given any more for slower motion.

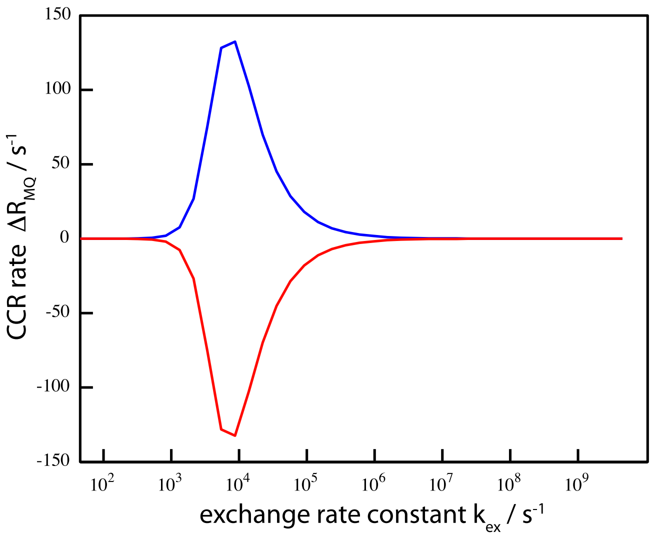

Figure S3. The sign of ΔR_{MQ} depends on the product of the signs of the chemical-shift differences $\Delta\nu_H$ and $\Delta\nu_N$. Shown in blue is a simulation equivalent to the blue curve in Figure S1. In red, the sign of the chemical-shift difference of one of the nuclei is inverted, i.e. $\Delta\nu_H$=-800Hz/ $\Delta\nu_N$=160Hz or $\Delta\nu_H$=800Hz/ $\Delta\nu_N$=-160Hz. The population of the minor state is 10%. The dipolar coupling and CSA parameters were as set in the simulations in Figure S1, and their orientation was fixed, i.e. did not alter upon exchange.

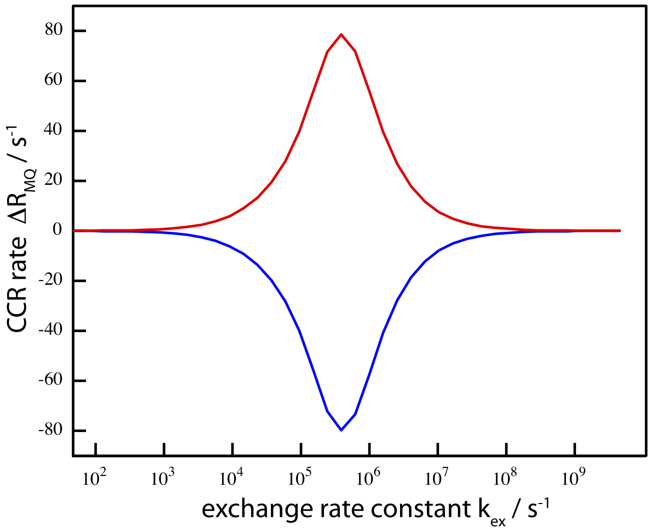

Figure S4. Negative values of ΔR_{MQ} can arise from anti-correlated motion of the CSA tensors, i.e. the sign of the angular change of the two tensor orientations is different. In the simulation shown in red, the angle β of the ^{1}H CSA is set to 10° in the major (90%) state A, and to 40° in the minor state, while the ^{15}N CSA is at 0° in state A and 30° in state B. In the simulation shown in blue, the angles in state A are identical to the ones above, but the angle of the ^{1}H CSA tensor in state B is set to β=-20°. Anisotropies of all tensors were identical to the ones in Figure S1.

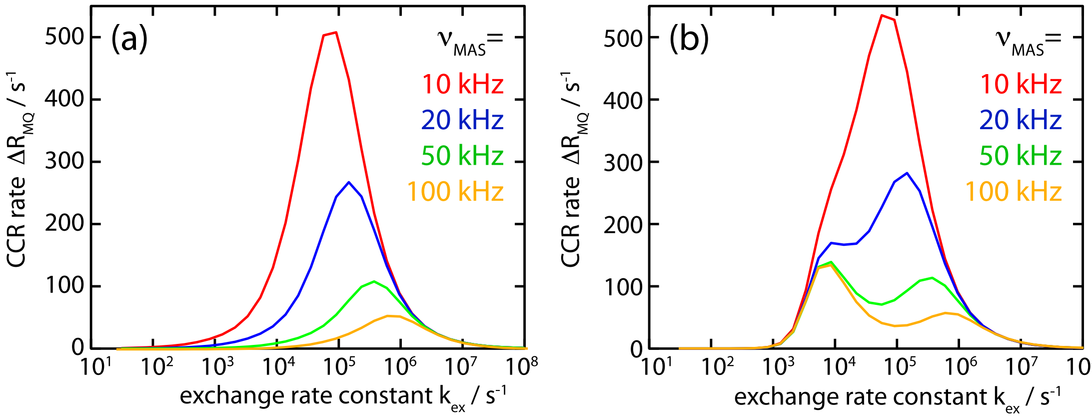

Figure S5. MAS dependency of the differential ZQ/DQ line broadening, resulting from correlated angular fluctuation of the two CSA tensors only (a), and fluctuation of the CSA tensors as well as isotropic chemical shifts (b). The CSA tensor parameters as well as the angle by which they were modulated (30°) were identical as those specified in the caption of Figure S1. These data show that the part of the differential ZQ/DQ line broadening that arises from the isotropic chemical shift does not change with MAS frequency (as confirmed by additional simulations containing only the CSI part, not shown). However, the contribution to differential line broadening arising from CSA interference is MAS dependent.

DETAILS OF THE PULSE SEQUENCES USED IN THIS WORK

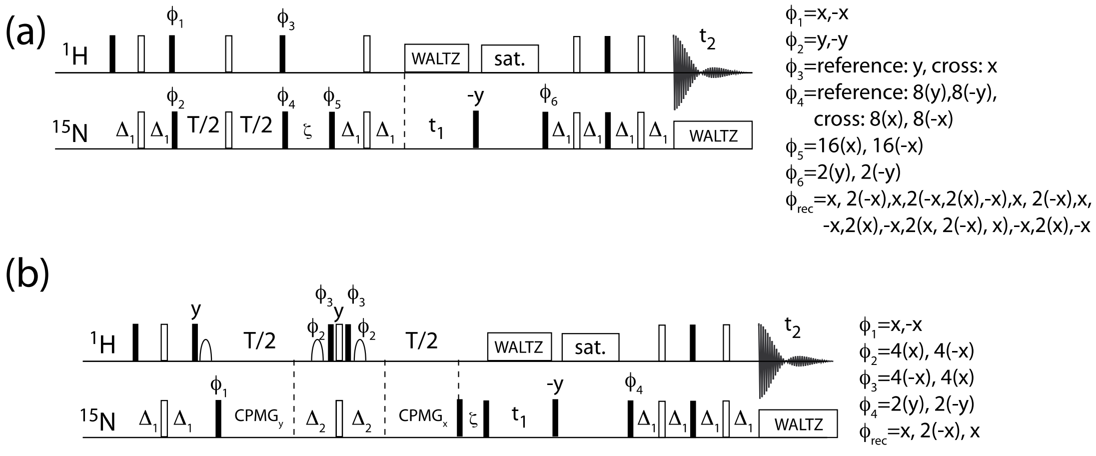

Figure S6. Pulse sequences and phase settings used in this study for measurement of (a) differential ZQ/DQ line broadening and (b) CPMG relaxation dispersion.

Filled (open) pulse symbols denote 90° (180°) pulses, and were applied at a field strength of γB_1=100kHz on both ^{1}H and ^{15}N, except for the ^{15}N pulses during CPMG pulse trains (denoted here only as "CPMG$_{y/x}$", where "x" and "y" denote the respective pulse phases of 180° pulses), which were applied at 10kHz. Pulse phases are as indicated on the right. Bell-shaped symbols in (b) denote water-selective sinc-pulses (truncated at first lobe) of 1.4ms duration. Delays were set to $\Delta 1$=2.3 ms, $\Delta 2$=2.677 ms, ζ=1ms in the experiment (a) and ζ=50ms in experiment (b). In (b), the total CPMG relaxation T was 30 ms in the experiments at 600MHz, and 20ms at 800MHz. Suppression of solvent ^{1}H signals was achieved using a circa 5kHz TPPM irradiation for 30 ms, as denoted by "sat." in the sequences. WALTZ decoupling was applied at 3kHz and 2.5kHz of ^{1}H and ^{15}N, respectively. Phase setting are indicated in the figure. Pulses for which no phases are specified were applied with phase x. Quadrature detection in t_1 was achieved by alternating ϕ5 in (a) and the pulse phase preceding t_1 in (b) according to the States-TPPI scheme.

SOLID-STATE MQC DECAY DATA

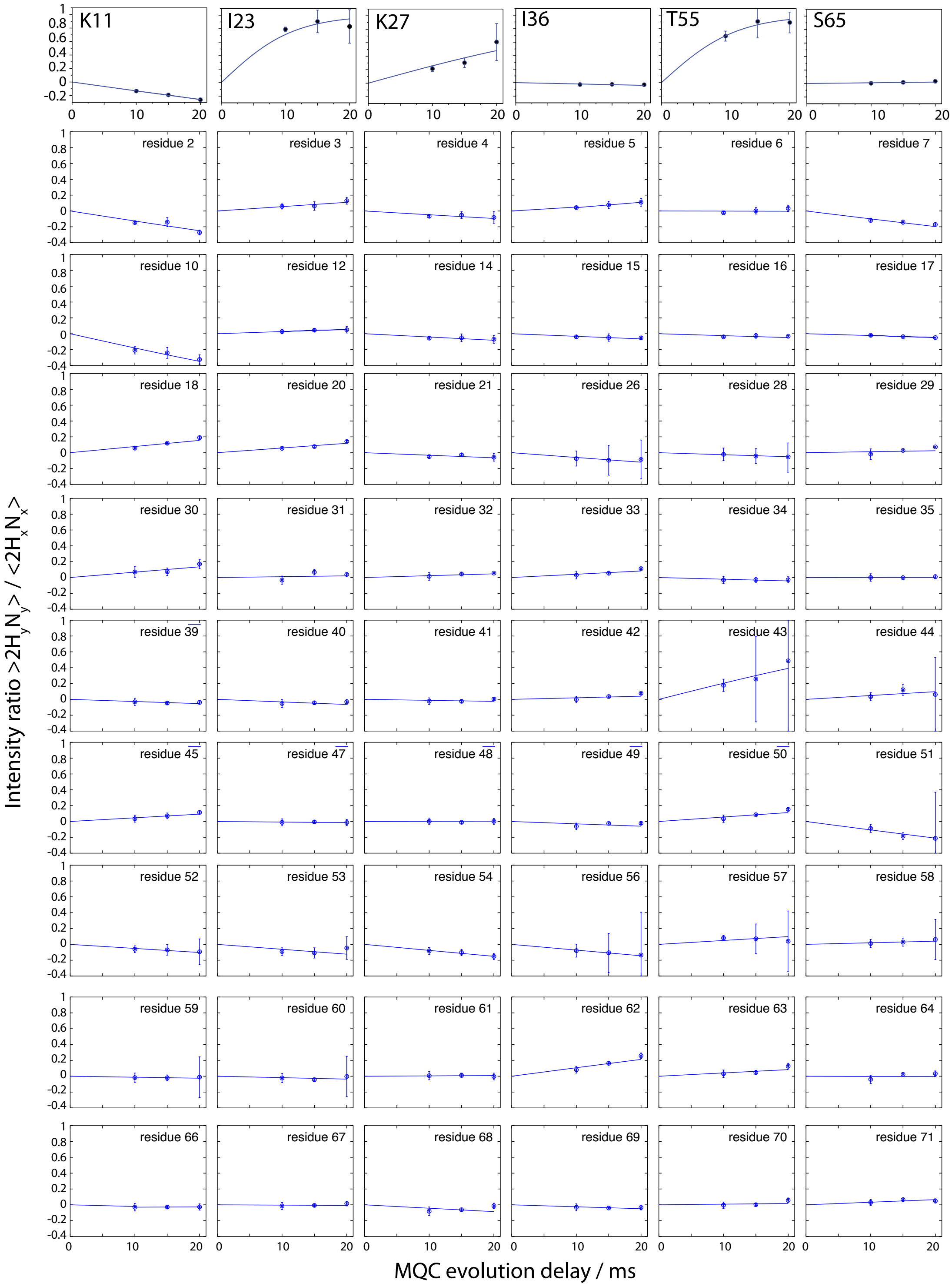

Figure S7. Residue-wise buildup-curves due to differential ZQ/DQ decay for all residues for which data are available. Data shown in the main paper are those in the top row.

INVESTIGATION OF THE USE OF ^{1}H DECOUPLING IN SOLID-STATE CPMG EXPERIMENTS

Two classes of approaches have been proposed in solution state for measuring ^{15}N CPMG RD experiments: (i) experiments that measure the average decay of in-phase ^{15}N coherence (N_x) and anti-phase coherence ($2H_zN_y$), as shown in Figure 3a, or (ii) an experiments measuring only the in-phase coherence, by applying ^{1}H decoupling during the relaxation delay.[4,12] This latter requires that the CW field strength on ^{1}H be adapted slightly for different CPMG frequencies, to ensure efficient and artifact-free decoupling.[4,13]

The latter should, in principle, be advantageous in terms of sensitivity here, because ^{15}N coherence life times are longer with ^{1}H decoupling.[4,12] We have investigated the feasibility of employing this latter scheme in the solid state.

However, as shown below in Figure S8, varying the ^{1}H cw field strength within the required range, as proposed by Hansen and Kay, leads to substantial variation of the ^{15}N decay rates, which can be understood as rotary resonance effects. Thus, this experiment is not directly transferable in a straightforward manner to MAS solids-state NMR, which prompted us to use scheme (a) in this study. We currently explore the possibility that by carefully choosing relaxation delays and CPMG frequencies, and ^{1}H rf field strengths, one may minimize the systematic errors. In-depth investigations of the practical applicability are outside the scope of the current study.

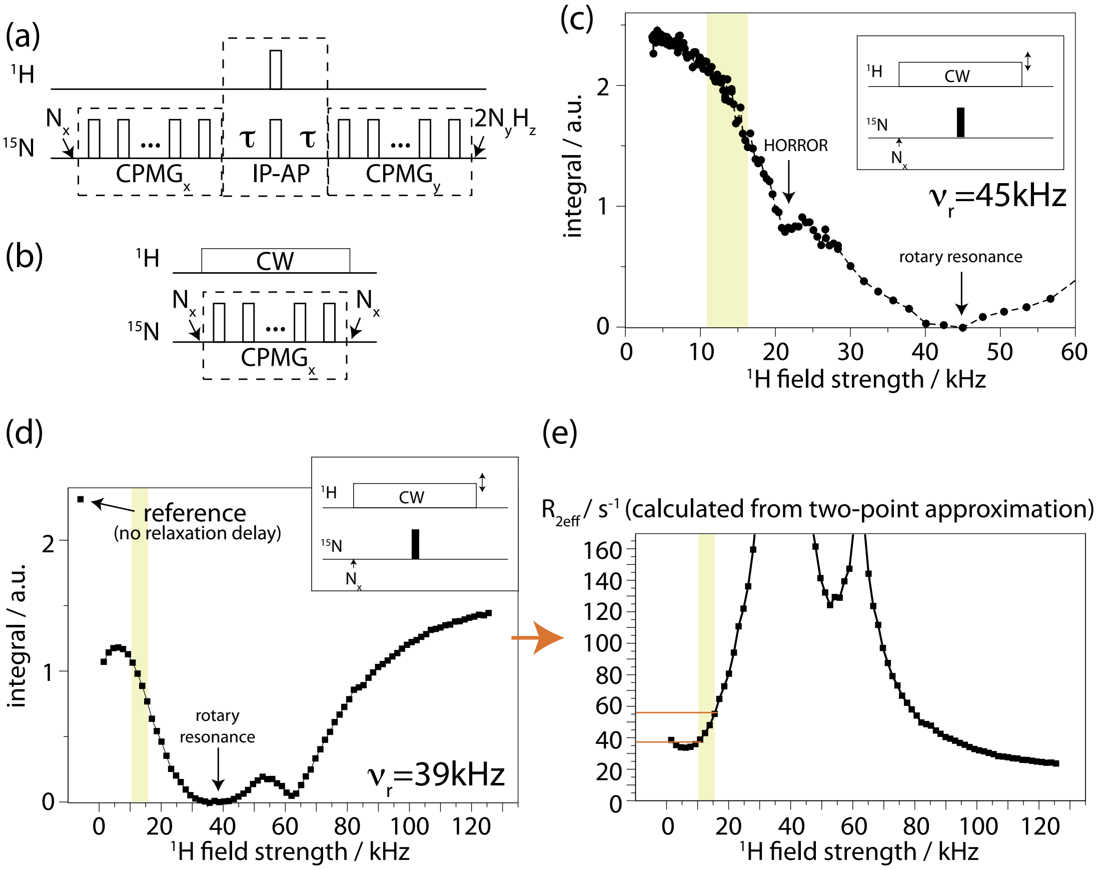

Figure S8. (a,b) Pulse sequences proposed for CPMG RD experiments in solution, comprising an in-phase-to-anti-phase (IPAP) conversion element, with the delay τ set to 1/(4J)[5,13] (a, "Loria-Palmer experiment"), or continuous-wave ^{1}H decoupling to prevent buildup of anti-phase (b, "Hansen-Kay experiment").[4] (c) Experimental investigation of the effect of ^{1}H cw decoupling on the decay of ^{15}N in-phase coherence on a highly deuterated sample (20% back-exchanged) of ubiquitin at 45kHz MAS. In the experiment, after preparation of a state corresponding to N_x using refocused INEPT, a 20ms transverse relaxation delay with a central π pulse on ^{15}N was applied with CW irradiation on protons. The remaining N_x coherence at the conclusion of this period was then detected by back-transfer to protons in a double-INEPT step, akin to previous experiments. The integral over the amide region (7 to 10ppm) is shown as a function of the ^{1}H irradiation field strength. Typically applied field strengths in the Hansen-Kay experiment are indicated in yellow, and these data show that the life time of ^{15}N coherence has a sharp dependence on the ^{1}H field in this range.

In (d) and (e) a similar experiment to the one in panel (c) was performed, with minor differences (CP steps instead of refocused INEPT). The experiment used a 30% ^{1}H-back-exchanged sample of otherwise deuterated ubiquitin, spinning at 39kHz MAS frequency in a 14.1 T (600MHz) B_0 field, using an Agilent 1.6mm Fast-MAS probe. (Thus, the protonation level here was higher than in the experiments shown in the main text, and MAS was slower.) As compared to the data in panel (c), a wider range of ^{1}H decoupling rf fields has been investigated, and a reference point without relaxation delay was included. The latter allows calculation of an effective decay rate R_{2eff} for each ^{1}H rf field strength, which are shown in (e). These R_{2eff} values show that when varying the ^{1}H rf field in the range of about 10-15kHz, which is the range of variation previously proposed in the "Hansen-Kay experiment", variations in R_{2eff} of about 20s^{-1} result. Such variations are incompatible with quantitative interpretation of CPMG data.

PROPERTIES OF SOLID-STATE CPMG FROM NUMERICAL SIMULATIONS

Here we investigate how CPMG relaxation dispersion profiles in a solid sample undergoing MAS may deviate from the ideal Bloch-McConnell case applicable in solution state.
The goal of this discussion is (i) to highlight through which mechanisms solid-state CPMG relaxation dispersions may be different from solution-state and (ii) to obtain realistic estimates how large these deviations are. We use numerical spin simulations, explicitly taking into account an exchange process, in order to derive an understanding as well as quantitative estimate of these effects. As shown below, there are indeed deviations from the simple Bloch-McConnell picture, which can be understood in terms of interference effects between various time-dependent processes. The deviations of the solid-state CPMG dispersions from those predicted by Bloch-McConnell treatment are generally within the experimental noise obtained in study, justifying the use of the Bloch-McConnell treatment to fit our data.

Unlike in solution state, anisotropic interactions (CSA, dipolar couplings) are present in the solid state. The periodic sample rotation (MAS) – the first time-dependent process we consider – renders these interactions time-dependent. In addition, the stochastic exchange process is another time-dependent process, rendering both the isotropic as well as the anisotropic interactions time dependent. Furthermore, the periodically applied π pulses constitute a third time-dependent process.

In principle, interference effects between all three time-dependent processes may arise. **(i)** Interference between CPMG pulses and the isotropic chemical shift fluctuation arising upon conformational exchange is giving rise to the Bloch-McConnell-type CPMG dispersions that are sought here. This is identical to solution state. As one may expect, this behavior is also found in a solid sample in the case of a two-spin system, where all interactions (CSA, dipole) stay fixed upon exchange, and therefore the MAS rotation eliminates these interactions irrespective of the dynamic process (Figure S9).

(ii) Interference between the π pulses and the MAS-modulation of CSAs and homonuclear dipolar couplings – in the absence of dynamics – are well known and are exploited in the RFDR and SEDRA experiments. (Gullion, T.; Vega, S. *Chem. Phys. Lett.* **1992**, *194*, 423-428.) These interferences arise when the rate at which pulses are applied matches the MAS frequency. In our case, however, we are far outside this regime, as the maximum CPMG frequency is of the order of 1kHz, while MAS was applied at 45 to 50kHz. Thus, we can neglect this effect (this can be demonstrated by numerical simulations with/without 15N-15N couplings and with/without 15N CSA; data not shown).

(iii) Interference between MAS and dynamics needs to be considered. Figure S10 shows numerical simulations of the Loria-Palmer CPMG relaxation dispersion experiment applied to a two-spin N-H system undergoing exchange between two conformations. The two states differ in their isotropic chemical shift, as well as the orientation of CSAs and dipolar coupling. As one can see from a comparison to the Bloch-McConnell treatment (solid lines), the jumps of the anisotropic interactions induce an additional contribution to R_{2eff}, that is almost (but not entirely, see below) independent of the CPMG frequency. This additional dephasing can be understood by the fact that the dynamic process prevents full MAS-averaging of the anisotropic interactions. Thus, as expected, this additional contribution to R_{2eff} must be dependent on the match between the rate of exchange and the MAS rate. This is indeed the case, as shown in Figure S11, where the additional contribution is determined for various MAS frequencies and exchange rate constants.

If this additional contribution to R_{2eff} was independent of the CPMG frequency, it would not have any impact on the applicability of the Bloch-McConnell treatment: any fitting of relaxation dispersion curves involves anyways an offset term, representing any decay not arising from fluctuation of isotropic chemical shift (e.g. Redfield relaxation). However, as shown in Figure S12, the additional contribution to R_{2eff} is not perfectly independent of the CPMG frequency. This slight dispersion of R_{2eff} as a function of the CPMG frequency, shown here for the case of zero isotropic chemical shift difference and only angular fluctuation of the N-H bond, is of the order of about $2s^{-1}$. It depends on the jump angle and the dipolar coupling and CSA parameters. In principle, one might take this effect into account when fitting relaxation dispersion curves by fitting the jump angle along with the usual exchange parameters.

(iv) Furthermore, we need to consider whether the application of CPMG pulses at varying rates has an impact on the coherent mechanisms of signal decay (i.e. even without dynamic processes). It is well known that coherent mechanisms dominate the decay in protonated samples. Most important in this context are dipolar couplings to the bath of proton spins. In highly deuterated samples (10% back-exchanged) , where the latter is greatly diluted, at fast MAS (60kHz), Lewandowski et al have recently roughly estimated that the remaining contribution from coherent mechanisms to decay is of the order of about $5\text{-}6s^{-1}$.[14] If this contribution varies as a function of ν_{CPMG}, then the Bloch-McConnell treatment is not strictly valid.

In order to investigate this, we have simulated 3-spin and 4-spin systems with additional protons, that undergo exchange. The results of these simulations, shown in Figure S13 and S14 are as follows. The contribution of couplings to remote spins further increases the effective decay rate (as expected, see Figure S13). However, this additional dephasing is not completely independent of the CPMG frequency (see Figure S14). This introduces artifacts into CPMG dispersion curves. As estimated from the 4-spin systems in Figure S14, these variations of R_{2eff} as a function of the CPMG frequency are on the order of up to $5s^{-1}$. This value may be seen as an upper estimate, because the simulated spin system contains two nearby protons, which are closer than the effective distances in a 20% back-exchange sample used in this study.

In order to determine what the effect of such variations would be on the extracted exchange parameters in this study, we have fitted such simulations, in the same way as the experimental data were fitted. The conclusion from these fits is that the systematic errors arising from coherent mechanisms are within the noise error levels (Table S1), and therefore in the present case not of major issue, although generally of potential relevance.

Finally, we experimentally estimate the systematic errors in CPMG curves (i.e. fluctuations of R_{2eff} with ν_{CPMG}. Two arguments can be invoked in favor of the above estimation that the systematic errors are of the order of $5s^{-1}$ at most. First, individual residue-wise CPMG curves are flat within error bar for many residues. SNR for individual residues is, however, such that flucutations of a few s^{-1} would not be visible. In order to increase SNR, we have measured the decay of bulk amides at different CPMG frequencies (Figure S15). These fluctuations, measured under conditions that are more unfavorable than those in the main paper (higher protonation, slower MAS) are indeed of the order of $5s^{-1}$. (Note that part of the apparent decrease of R_{2eff} with νCPMG may actually result from contributions of those residues that have conformational exchange.)

Taken together, we identified mechanisms that make the Bloch-McConnell treatment not rigorously applicable: (i) there is an interference between the three time-dependent processes, leading to a slight dispersion of $R_{2\mathrm{eff}}$, as shown in Figure S11, and (ii) the decay induced by coherent mechanisms is not independent of the CPMG frequency. We estimate the resulting systematic error in $R_{2\mathrm{eff}}$ values to be below about 5s^{-1}.

Finally, we stress the fact that any contribution to $R_{2\mathrm{eff}}$ that is independent of the CPMG frequency is irrelevant for practical purposes, as the plateau value of $R_{2\mathrm{eff}}$ is a fit parameter with hardly interpretable physical meaning. Thus, the fact that the plateau values (i.e. $R_{2\mathrm{eff}}$ at high CPMG frequencies) is not free of coherent mechanisms of signal decay does not interfere with quantitative interpretation.

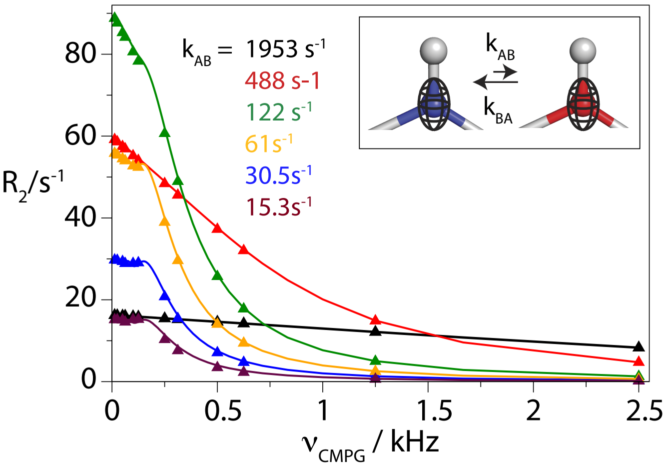

Figure S9. Relaxation dispersion in a solid sample (2-spin system) undergoing exchange between conformations with fixed bond orientations. The effective relaxation decay $R_{2\mathrm{eff}}$, is shown for the case of explicit solid-state simulations (triangles) and compared to solutions of the Bloch-McConnell equations (solid lines). In all cases the population of the minor state was set to 10%, and the chemical shift difference $\Delta\omega_{AB}$ was 300 Hz. Different exchange rate constants between the major (A) and minor (B) conformation are shown, as indicated. These data show that in the case of a two-spin system, without any angular fluctuations of the dipolar coupling/CSA, MAS fully eliminates the effect of these anisotropic interactions, resulting in a behavior that is fully identical to solution state.

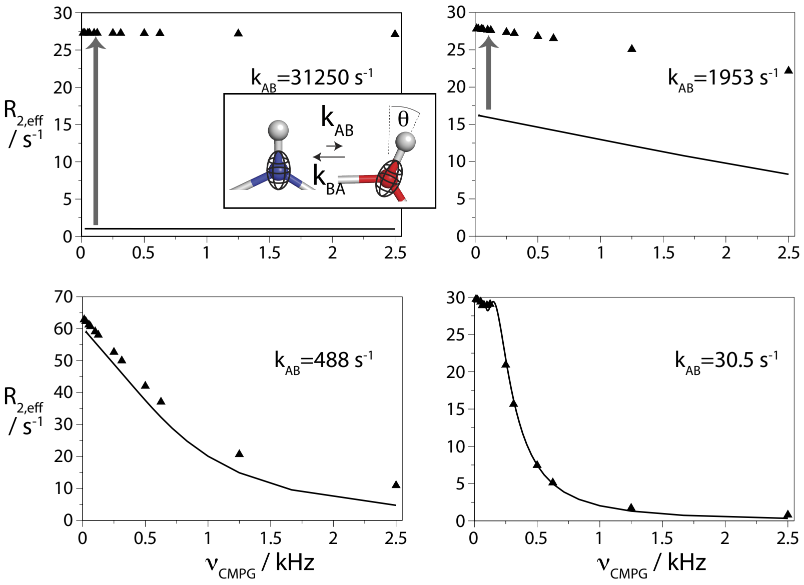

Figure S10.
Effective coherence decay rate constant in a two-spin system (A<->B) undergoing fluctuation of the isotropic chemical shift as well as angular fluctuation of the CSA and dipole tensors, as indicated by the inset. These data (triangles) are compared to solution-state-type Bloch-McConnell results (solid lines). Arrows highlight the apparent additional, solid-state specific contribution to R_{2eff}. Exchange parameters: $\Delta\omega_{AB}$=300Hz, p_B=10%). The jump angle θ was set to 20°. This offset can be understood as an interference with MAS, shown below.

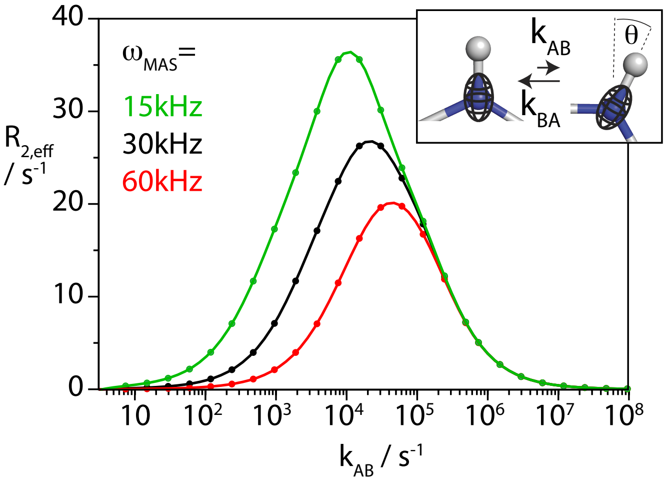

Figure S11. Illustration of the solid-state specific additional contribution to R_{2eff}, resulting from modulation of anisotropic interactions (this is the additional contribution to R_{2eff} indicated in Figure S10 with vertical arrows). The effective coherence decay rate constant at the lowest available CPMG frequency is shown for different MAS frequencies. The exchange scenario in the inset was used with θ=20° and p_B=10%, and the difference of the isotropic chemical shift between the two states was set to Δω=0 (non-zero values only lead to the trivial Bloch-McConnell-type dispersion, which we wanted to remove here for clarity). Simulation data (circles) for three different MAS frequencies are shown. Solid lines are smooth lines (cubic spline) to the simulated data.

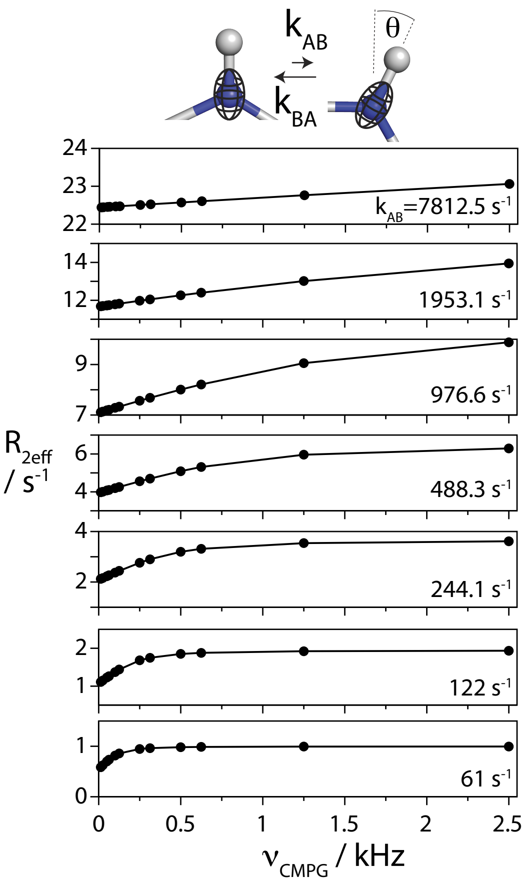

Figure S12. Close inspection of the interference between modulation of anisotropic interactions and CPMG pulses in a rotating solid. The orientation of the CSA and dipolar coupling tensor was assumed to undergo 20° jumps upon the dynamic process, as depicted on the top. The chemical shift of the two conformations, populated to 90% and 10%, respectively, was assumed to be identical, in order to eliminate the Bloch-McConnell part to the dispersion. Exchange rate constants from the major state A to the minor state B are indicated in the individual panels.

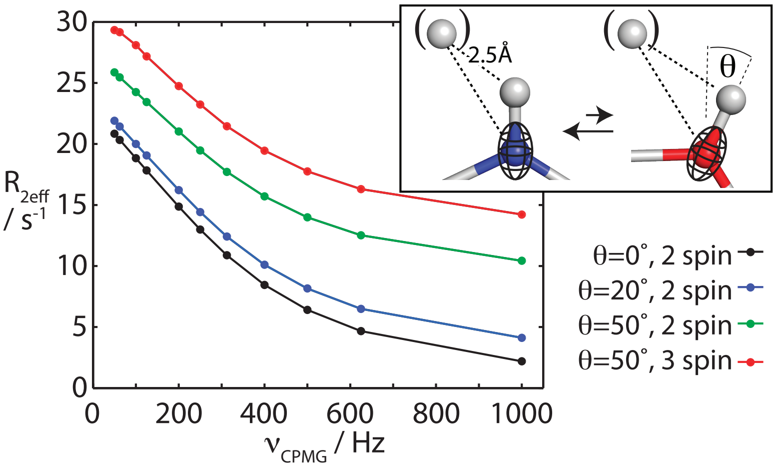

Figure S13. Simulated CPMG RD curves in a sample undergoing MAS, and an exchange process involving modulation of the isotropic chemical shift, as well as modulation of the orientation of CSA and dipole tensors. The exchange parameters in the simulations are p_B=10%, k_{ex}=2112s^{-1}, Δω=1.51ppm (at 800MHz; this corresponds to the values found for K27); jumps of the orientation of the CSA tensor (axially symmetric, Δσ=170ppm, collinear with N-H bond) and the N-H dipole (δ_D=22.5kHz) by an angle θ, as well as a remote proton (angle N-H-H=135°) are taken into account as indicated in the insert and legend. For the three-spin system, the chemical shift difference between the two protons was set to zero. This is overly simplistic, and Figure S14 shows then a more realistic scenario.

The black curve (fixed angle) is identical to the Bloch-McConnell solution. Jumps by θ (≠0°) lead (i) to a general increase of R_{2eff} because MAS averaging of dipolar coupling and CSA are not perfect any more (see Figure S10/S11) and (ii) to a slight reduction of the apparent amplitude of the dispersion (i.e. the difference between the first and last point; see Figure S12). Based on similar arguments, the remote spin leads to further increase in R_{2eff}. In this particular case of zero frequency difference between the protons, this increase is essentially ν_{CPMG}-independent, but in the general case (see figure S14) it is not. Best-fits to these simulations (Bloch-McConnell) are shown in Table 1.

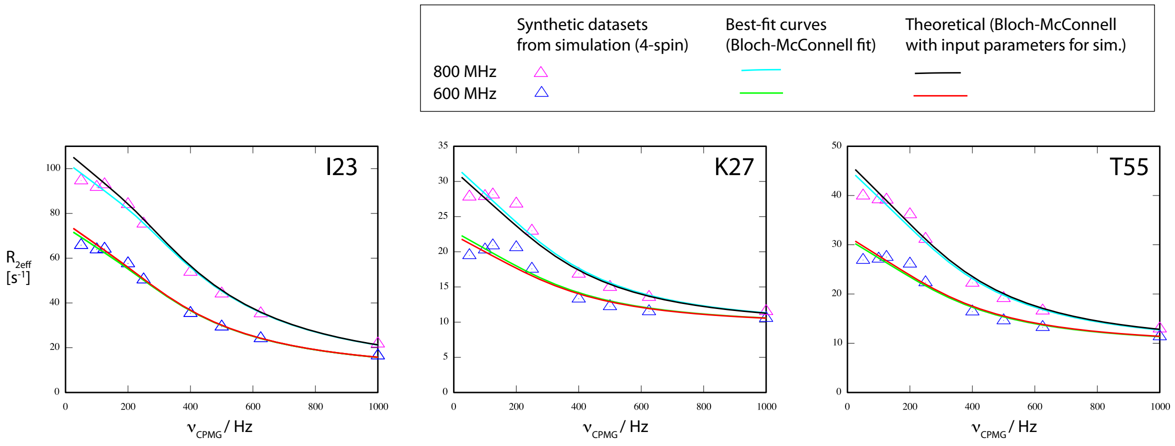

Figure S14. Simulations of three exchanging four-spin systems undergoing the CPMG pulse sequence. The three panels correspond to different ^{15}N chemical shift differences between the exchanging states Δω, which were set to the values found in ubiquitin for I23, K27 and T55. In all cases, a directly bonded N-H(1) pair as well as two remote protons were assumed. In the major state, proton H(2) was placed at 2.5Å distance, as in Figure S13, H(3) was placed at 3.1Å relative to the H(1) and at 6.5Å relative to H(2). The position of the remote ^{1}H spins was kept constant upon the exchange process, and the N-H bond (and CSA's) were undergoing a 50-degree jump upon exchange (similar to Figure S13). All H-H and H-N dipolar couplings as well as CSA's were taken into account, as above. The ^{1}H isotropic chemical shifts were set to 150Hz (H1), 350Hz (H2) and 0Hz (H3). A constant-time relaxation delay of 40ms was used, and 9 CPMG frequencies were simulated (the choice of which is dictated by timing issues of rotor synchronization and CT delay). Data are shown from two field strengths. Best-fit curves (Bloch-McConnell treatment) as well as theoretical curves (i.e. assuming Bloch-McConnell behavior and the actual exchange parameters that served as input to the simulations) are shown.

The best-fit values are shown in Table S1 (row 8); all best-fit values agree with the input values within a range that is smaller than the random error in this study.

Table S1.

	Simulation, parameters	fitted k_{ex} / s^{-1}	fitted p_E / %	fitted Δω, I23 /ppm	fitted Δω, K27 /ppm	fitted Δω, T55 /ppm
1	fixed bond angle, two-spin	2112	9.99	3.78	1.51	1.97
2	jump by θ=20°, two-spin,	2176	9.91	3.77	1.48	1.95
3	jump by θ=50°, two-spin, blue curve in S13	2174	9.73	3.73	1.38	1.88
4	jump by θ=90°, two-spin	2094	9.60	3.71	1.33	1.84
5	jump by θ=20°, three-spin	2070	9.97	3.82	1.47	1.94
6	jump by θ=50°, three-spin, red curve in S13	2168	9.93	3.70	1.35	1.85
7	jump by θ=90°, three-spin	2224	9.81	3.67	1.31	1.83
8	4-spin system, θ=50°, see Figure S14.	2088	9.02	3.99	1.60	2.07

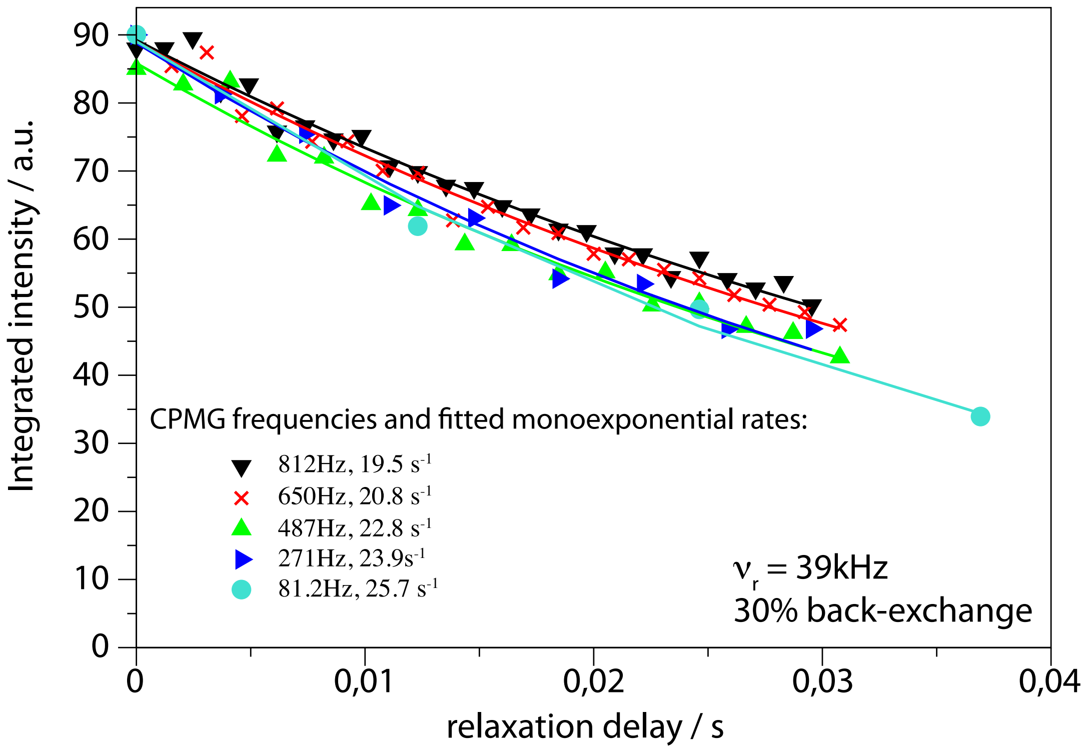

Figure S15. Experimental decay curves of the bulk amide signals over time, over the course of the ^{15}N CPMG pulse sequence (Loria-Palmer experiment). The sample used here was 30% back-exchanged deuterated ubiquitin (i.e. slightly higher 1H content than the sample used otherwise), and the MAS frequency was 39kHz (i.e. slightly lower than all other data). Both factors are expected to lead to less favorable properties. Mono-exponential rate constants are shown, and the spread between these rate constants over a range of CPMG frequencies is of the order of 5s^{-1}, i.e. typically within error margins of individual residues in our study.

EXPERIMENTAL SOLID-STATE CPMG DATA

Bloch-McConnell fit of CPMG relaxation dispersion data

Fitting of the experimental CPMG relaxation dispersion curves was performed using numerical integration of the Bloch-McConnell equation. The fitting routine was implemented in MATLAB, and exploited MATLAB's non-linear least-squares fitting tools. The implicit assumptions are that pulses are infinitely short, that the intrinsic relaxation rate constant (at infinite CPMG frequency, $R_{i\infty}$ below) are identical in the two states, and that differences in the decay of in-phase and anti-phase coherence are eliminated, which is strictly valid in the Loria-Palmer experiment in solution state. While this is a standard and oft-used procedure in solution-state CPMG analyses, we show the equations here for completeness.

Magnetization evolves during delays between consecutive pulses under the action of the isotropic chemical shift (R_{CS}), two-site exchange (R_{ex}) and transverse decay (e.g. Redfield relaxation, R_R), as follows:

$R = R_{CS} + R_R + R_{ex}$, where

$$R_{CS} = -i\begin{pmatrix} \omega_A & 0 \\ 0 & \omega_B \end{pmatrix}, R_R = -\begin{pmatrix} R_{A\infty} & 0 \\ 0 & R_{B\infty} \end{pmatrix}, R_{ex} = -\begin{pmatrix} k_{AB} & -k_{BA} \\ -k_{AB} & k_{BA} \end{pmatrix}.$$

Here ω indicates isotropic chemical shift, $R_{i\infty}$ is the R_2 decay at infinite CPMG frequency (i.e. an offset term, containing Redfield relaxation and possibly other decay contributions); $R_{A\infty}$ and $R_{B\infty}$ were assumed to be equal. k_{ij} is the rate constant for exchange from state i to state j. The propagator describing the evolution of the initial vector of magnetization over the unit element of the Loria-Palmer sequence, i.e. τ-π-τ-τ-π-τ (taking into account that it is applied before and after the in-phase-to-anti-phase element) is given as

$U = \exp(R\tau)\cdot\exp(2\overline{R}\tau)\cdot\exp(R\tau)$, where $\overline{R}$ is the complex conjugate of R.

The evolution of the initial vector of ^{15}N magnetization $M(0) = M_0\begin{pmatrix} p_A \\ p_B \end{pmatrix}$ up to the total relaxation delay T_C is calculated by applying the above propagator U a number of times to $M(0)$, according to the number of τ-π-τ-τ-π-τ cycles within the constant delay T_C.

The effective decay rate constant R_{2eff} for a given CPMG frequency is then obtained as $R_{2eff} = -\frac{1}{T_C}\cdot\ln\left((M_A + M_B)/M_0\right)$, where M_A and M_B are the two components of $M(T_C)$. Non-linear least square minimization of chi-square between the experimental values of R_{2eff} and the calculated R_{2eff} profile in MATLAB (using the fminsearch routine) is used to obtain best-fit values of kinetic rates, populations and chemical shift differences.

Random error (chi-square plot) of the CPMG fit

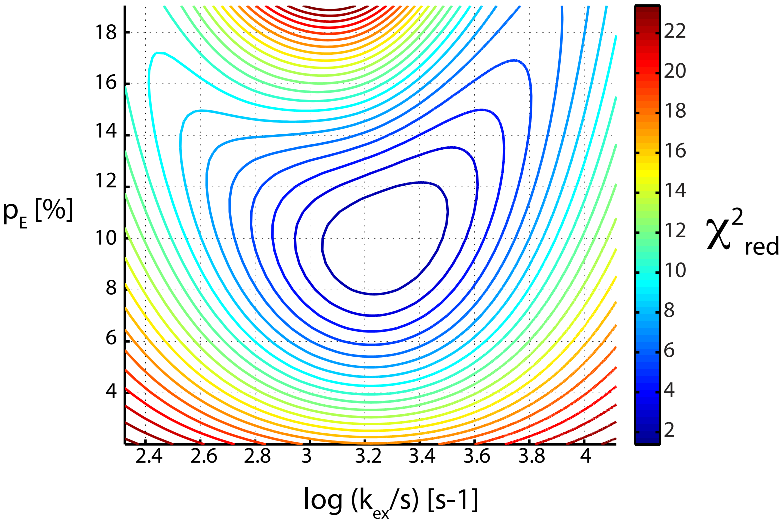

Figure S16. Plot of the reduced chi-square obtained in the fit of the CPMG data of I23, K27 and T55, as a function of the rate constant and minor-state population. Contour lines are drawn in steps of $\Delta\chi^2_{red}$=1 , with the innermost surface being at the minimal χ^2_{red}+1. The minimal χ^2_{red} (i.e. the χ^2_{red} for the reported best-fit values of exchange parameters) was 1.38. These data show that exchange rates as observed in solution (tens of microseconds even at 20K lower temperature) are clearly outside the confidence interval of our fit.

Asymmetric error bars of R_{2eff}

The error bars of R_{2eff} values shown in Figure 3 in the main paper are slightly asymmetric. The origin of this asymmetry is shown below, with the example of Ile23. As seen from 1D spectral traces, the cross peaks of Ile23 for the lowest CPMG frequencies are very close to the noise level, reflecting the strong exchange-induced line broadening. The value of R_{2eff} is determined from the intensity ratio in a reference experiment (without relaxation delay) and one with relaxation delay. The reported error margins were determined from Monte Carlo runs, in which the intensity of the spectrum with relaxation delay was randomly varied according to twice the spectral noise (synthetic data sets). In those Monte Carlo runs for which the synthetic intensity was smaller than the experimental one (thus approaching zero), R_{2eff} tends to very large values, as the denominator gets very small. The functional form therefore explains why error bars are asymmetric, particular for those cases where cross peaks are very weak.

We preferred, thus, to report asymmetric error bars in Figure 3, as they reflect more accurately the actual situation. Error bars of the exchange parameters were obtained by performing a Monte Carlo analysis of the Bloch-McConnell equations to the experimental CPMG relaxation dispersion data. For these Monte Carlo runs, we used the asymmetric error bars on R_{2eff}, as just explained. The resulting error bars on the exchange parameters are, however, essentially symmetric (see Figure S9). We want to stress also that a separate analysis of the CPMG data that assumed symmetric error margins on R_{2eff} leaded to very similar final error bars on the exchange parameters.

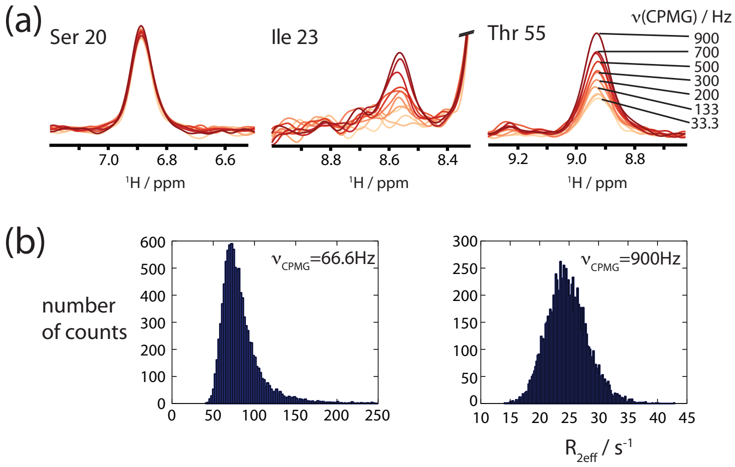

Figure S17. Origin of asymmetric error bars on R_{2eff} values. (a) 1D traces through three cross peaks in the data set collected at 600MHz. The intensity of Ile23 is close to the noise level for the lowest CPMG frequencies. (b) Histograms of calculated values of R_{2eff} in 10000 Monte Carlo runs for Ile23, in which the cross peak intensity was varied within twice the spectral noise and the R_{2eff} values calculated from the ratio of this intensity and the reference intensity. In the left panel, corresponding to 66.6Hz CPMG frequency, the distribution is clearly asymmetric, while in the right panel the distribution is much more symmetric, which is a consequence of the higher SNR of this cross peak.

Residue-wise CPMG RD curves for all resolved peaks in microcrystalline ubiquitin

Figure S18 (below) shows CPMG RD data for all observed residues in microcrystalline ubiquitin, recorded at 600MHz (red) and 800 MHz (black).

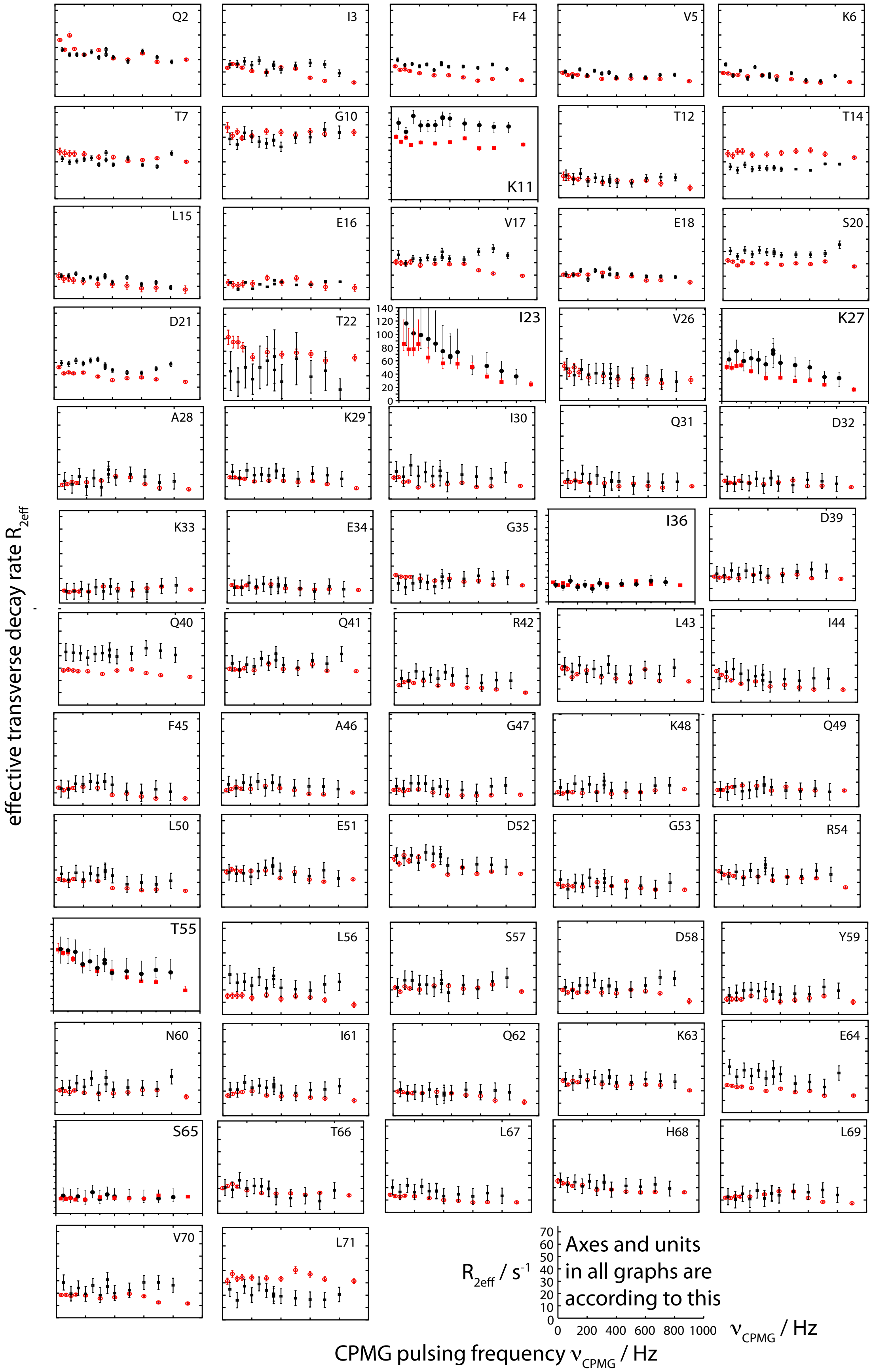
Q2
I3
F4
V5
K6
T7
G10
K11
T12
T14
L15
E16
V17
E18
S20
D21
T22
I23
140
120
100
80
60
40
20
0
V26
K27
A28
K29
I30
Q31
D32
K33
E34
G35
I36
D39
Q40
Q41
R42
L43
I44
F45
A46
G47
K48
Q49
L50
E51
D52
G53
R54
T55
L56
S57
D58
Y59
N60
I61
Q62
K63
E64
S65
T66
L67
H68
L69
V70
L71
effective transverse decay rate R_{2eff}
R_{2eff} / s^{-1}
70
60
50
40
30
20
10
0
0 200 400 600 800 1000
ν_{CPMG} / Hz
Axes and units in all graphs are according to this
CPMG pulsing frequency ν_{CPMG} / Hz

Figure S18.

CHEMICAL SHIFT DIFFERENCE FOR AMIDE PROTONS

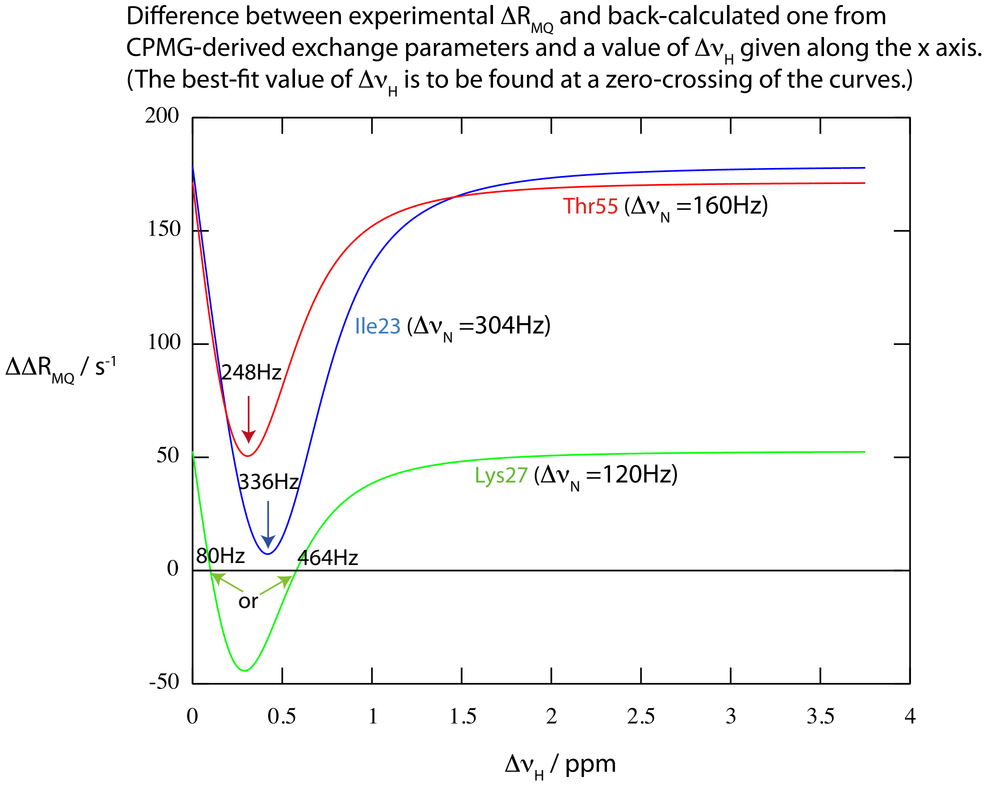

Difference between experimental ΔR_{MQ} and back-calculated one from CPMG-derived exchange parameters and a value of $\Delta\nu_H$ given along the x axis. (The best-fit value of $\Delta\nu_H$ is to be found at a zero-crossing of the curves.)

Figure S19. Determination of the chemical shift difference $|\Delta\omega_{AB}|$ for amide protons of residues I23, T55, K27. Shown is the difference between the experimental value of ΔR_{MQ}=179±47, 53±16 and 172±44 s^{-1} and the calculated value, based on the experimentally determined values of k_{ex}, p_B (common to all) and the ^{15}N chemical shift difference (for each residue). The calculation only takes into account the isotropic chemical shift, and was determined using equation 8 from reference 1. Best-fit values of $|\Delta\omega_{AB}|$ (^1H) are in the range of 0.5ppm or less in all cases. Of note, taking into account the isotropic chemical shift as the sole mechanism, the experimental ΔR_{MQ} cannot be fully explained, in particular for T55. This suggests partial contribution via the CSA/CSA mechanism.

SOLUTION-STATE MQC DECAY AND CPMG DATA

Here we show that the exchange process observed in the microcrystalline state is different from what is observed in solution, even if the solution conditions are similar to the solution from which crystals were obtained. For crystallization, ubiquitin was dissolved in 37µl of buffer A (20mM ammonium acetate, pH 4.3) at a concentration of 20mg/ml, then 14µl of a 40:60 v:v mixture of buffer B (50mM citrate, pH 4.3) and methyl-pentane-diol (MPD) was added, and the solution was placed in sitting drop crystallization plates. The mother liquor in the wells of these sitting drops was the above 40:60 mixture of buffer B and MPD. Thus, the concentration of MPD in the solution from which crystallization occurred was, at most, 60%. We have measured MQC decay experiments and CPMG relaxation dispersions at different conditions up to 45% MPD, as shown below. We do not see any detectable exchange process in such samples.

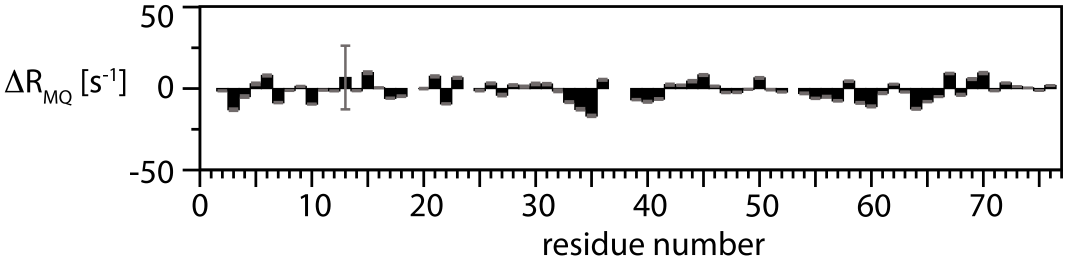

Figure S20. Solution-state ΔR_{MQ} values, obtained at 18.8T and 300K sample temperature. The data were obtained from a single delay value of T=20ms, using the experiment proposed by Kloiber and Konrat[5].

(a) in buffer at pH 4.3

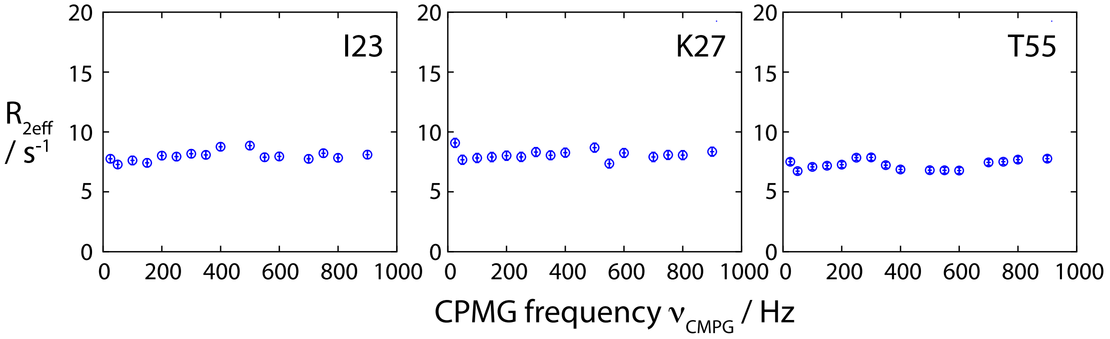

(b) with addition of MPD (25% v/v)

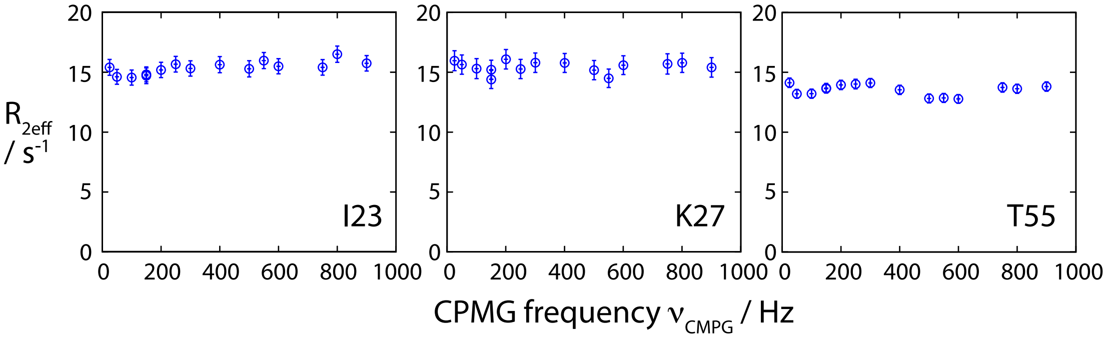

(c) with addition of MPD (45% v/v)

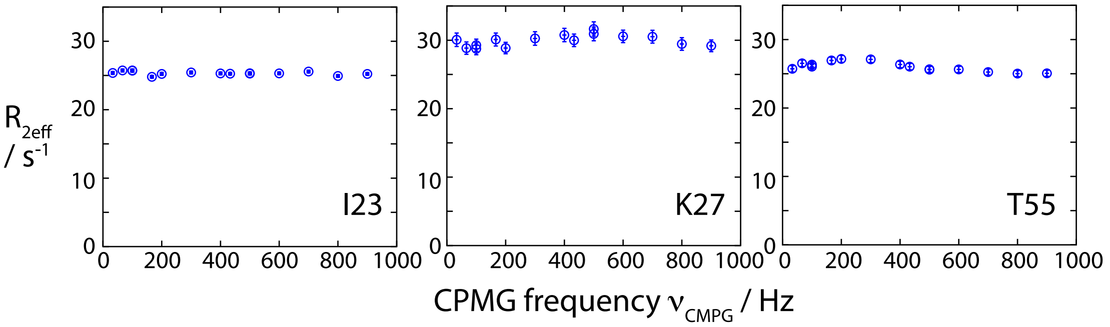

Figure S21. Solution-state CPMG RD data, obtained at a B_0 field of 14.1T, using the sequence proposed by Tollinger *et al.*[2,3,15] Note that while the dispersions for these three residues are flat in solution, they display very strong exchange broadening in the solid state. These data are in agreement with previous $T_{1\rho}$ dispersion experiments that showed that the exchange process is very fast in solution.

The top row shows data that were measured in the buffer in which ubiquitin was also dissolved for crystallization (20mM ammonium acetate, pH 4.3). For experiments in the bottom row, additionally the crystallization agent MPD was added to 25% and 45% (v/v). This leads to higher viscosity (as seen by increased R_{2eff} rates), but there is no exchange process visible.

REFERENCES

(1) Wang, C.; Palmer, A. *J Biomol NMR* **2002**, *24*, 263–268.
(2) Loth, K.; Pelupessy, P.; Bodenhausen, G. *J Am Chem Soc* **2005**, *127*, 6062–6068.
(3) Tjandra, N.; Bax, A. *J Am Chem Soc* **1997**, *119*, 8076–8082.
(4) Hansen, D. F.; Vallurupalli, P.; Kay, L. E. *J Phys Chem B* **2008**, *112*, 5898–5904.
(5) Kloiber, K.; Konrat, R. *J Biomol NMR* **2000**, *18*, 33–42.
(6) Frueh, D. *Prog Nucl Mag Res Sp* **2002**, *41*, 305–324.
(7) Tessari, M.; Vuister, G. W. *J Biomol NMR* **2000**, *16*, 171–174.
(8) Lipari, G.; Szabo, A. *J Am Chem Soc* **1982**, *104*, 4546–4559.
(9) Torchia, D.; Szabo, A. *J Magn Reson* **1982**, *49*, 107–121.
(10) Schanda, P.; Meier, B. H.; Ernst, M. *J Am Chem Soc* **2010**, *132*, 15957–15967.
(11) Giraud, N.; Blackledge, M.; Goldman, M.; Bockmann, A.; Lesage, A.; Penin, F.; Emsley, L. *J Am Chem Soc* **2005**, *127*, 18190–18201.
(12) Schanda, P.; Huber, M.; Verel, R.; Ernst, M.; Meier, B. H. *Angew Chem Int Ed Engl* **2009**, *48*, 9322–9325.
(13) Loria, J.; Rance, M.; Palmer, A. *J Am Chem Soc* **1999**, *121*, 2331–2332.
(14) Lewandowski, J. R.; Sass, H. J.; Grzesiek, S.; Blackledge, M.; Emsley, L. *J Am Chem Soc* **2011**, *133*, 16762–16765.
(15) Tollinger, M.; Skrynnikov, N.; Mulder, F.; Forman-Kay, J.; Kay, L. *J Am Chem Soc* **2001**, *123*, 11341–11352.